

1 **How do are the gravity waves triggered by a typhoon propagate**
2 **from the troposphere to the upper atmosphere?**

3 Qinzeng Li¹, Jiyao Xu^{1,2}, Hanli Liu³, Xiao Liu⁴, Wei Yuan¹

4 ¹State Key Laboratory of Space Weather, National Space Science Center, Chinese Academy of
5 Sciences, Beijing, 100190, China,

6 ²School of Astronomy and Space Science, University of Chinese Academy of Science, Beijing,
7 100049, China,

8 ³High Altitude Observatory, National Center for Atmospheric Research, Boulder, CO
9 80307-3000, USA,

10 ⁴School of Mathematics and Information Science, Henan Normal University, Xinxiang, 453007,
11 China,

12

13 Correspondence to: xujy@nssc.ac.cn

14 **Abstract**

15 Gravity waves (GWs) strongly affect atmospheric dynamics, and photochemistry, ~~as~~
16 ~~well as~~ and the coupling between the troposphere, stratosphere, mesosphere, and
17 thermosphere. ~~Also~~ In addition, GWs generated by strong disturbances in the troposphere
18 (~~such as~~ e.g., thunderstorms, ~~and~~ typhoons, ~~etc.~~) can affect the atmosphere of the Earth
19 ~~ranging~~ from the troposphere to the thermosphere. However, the fundamental process of GW
20 propagation from the troposphere to the thermosphere is poorly understood because it is
21 challenging to constrain this process ~~by using~~ observations. Moreover, GWs tend to
22 dissipate rapidly in the thermosphere because the molecular diffusion increases
23 exponentially. In this study, a double-layer airglow network ~~is~~ was used to capture ~~the~~
24 concentric ~~gravity waves~~ GWs (CGWs) over China, ~~which that~~ were excited by the Super
25 Typhoon Chaba (2016). We used ~~the~~ ERA-5 reanalysis data and Multi-functional Transport
26 Satellite-1 Observations ~~and to~~ quantitatively ~~described~~ the physical mechanism of
27 typhoon-generated CGWs propagating throughout the stratosphere, mesosphere, and
28 thermosphere. We found that the CGWs in the mesopause region were generated directly by
29 the typhoon in the troposphere. However, like the relay, the backward ray tracing analysis
30 suggested that CGWs in the thermosphere originated from the secondary waves generated
31 by the dissipation of the CGW and/or nonlinear processes in the mesopause region, ~~thereby~~
32 ~~resembling the relay in the context~~.

33 1. Introduction

34 Gravity waves (GWs) can transfer momentum and energy from the lower to upper
35 atmospheres, thereby affecting ~~the~~ global circulation and thermal structures, ~~as well as~~ and
36 the distribution of chemical composition in the middle and upper atmospheres (Holton, 1983;
37 Fritts and Alexander, 2003). Studies on The dynamic, photochemical, and electrodynamic
38 processes have indicated that GWs are fundamental for the coupling process between the
39 troposphere, stratosphere, mesosphere, and thermosphere (Liu and Vadas, 2013; Smith et al.,
40 2013; Vadas and Liu, 2013; Xu et al., 2015; Vadas and Becker, 2019).

41 Concentric GWs (CGWs) are a unique type of GWs ~~that are~~ considered to be mainly
42 generated by convective ~~activities~~ activity in the troposphere. CGWs can also be generated
43 by primary wave breaking (Vadas and Becker, 2019; Lund et al., 2020; Kogure et al., 2020)
44 volcanoes (Duncombe, 2022), nuclear explosions (Pfeffer and Zarichny, 1962; Pierce et
45 al., 1971), and rockets (Liu et al., 2020). CGWs in the stratosphere and mesosphere generated
46 by thunderstorms have been widely reported since their sources are ubiquitous (Taylor and
47 Hapgood, 1988; Sentman et al., 2003; Suzuki et al., 2007; Yue et al., 2009; Vadas et al., 2012;
48 Xu et al., 2015; Heale et al., 2019; Smith et al., 2020) ~~have been widely reported since their~~
49 ~~sources are ubiquitous~~. In previous studies, CGWs induced by typhoons were detected using
50 ground-based optical remote sensing (Suzuki et al., 2013) while those induced by hurricanes
51 and tropical cyclones were detected using the Suomi National Polar-orbiting Partnership
52 satellite (Yue et al., 2014; Xu et al., 2019) in the mesopause region.

53 Notably, GWs tend to dissipate rapidly in the upper atmosphere due to molecular
54 viscosity and thermal diffusion (Vadas, 2007). Thermosphere GWs that are not dissipated

55 can originate directly from the troposphere (Vadas, 2007; Azeem et al., 2015) or from
56 secondary GWs, which are generated ~~as a result of~~ from the breaking of primary GWs in the
57 mesosphere or thermosphere region (Vadas and Fritts, 2003; Vadas and Crowley, 2010;
58 Vadas and Azeem, 2021). Furthermore, Vadas and Becker (2019) for the first time presented
59 global simulations of tertiary CGWs from the dissipation of secondary CGWs in the
60 thermosphere. Moreover, wave-wave, wave-mean flow, self-acceleration, and nonlinear
61 breaking ~~also signify~~ are other potential secondary wave generation mechanisms (Lund and
62 Fritts, 2012; Fritts et al., 2015; Dong et al., 2020; Fritts et al., 2020; Franke and Robinson,
63 1999; Zhou et al. 2002; Heale et al. 2020). At the same time, tunneling has been deemed as a
64 mechanism that can couple waves from tropospheric sources to the thermosphere (~~e.g.~~
65 Walterscheid and Hecht, 2003; Gavrilov and Kshevetskii; 2018, Heale et al., 2021).
66 However, the lack of observations of the entire atmosphere limits our understanding of the
67 fundamental process of how ~~the~~ GWs propagate from the lower atmosphere to the upper
68 atmosphere step by step on the aspect of observations.

69 This paper presents a case study examining CGWs excited by Super Typhoon Chaba
70 (2016). This study examined the CGWs excited by Super Typhoon Chaba (2016) as a study
71 ease. To this end, we utilized Multi-functional Transport Satellite-1R (MTSAT-1R)
72 observations, multi-layer European Centre for Medium-range Weather Forecasts (ECMWF)
73 ERA-5 reanalysis data (Hoffmann et al., 2019; Hersbach et al., 2020), and high
74 ~~spatio~~o-temporal resolution double-layer airglow network (DLAN) (Xu et al., 2021)
75 observations. The CGW observations from the troposphere to the stratosphere and then to
76 the mesosphere were taken from MTSAT-1R, ERA-5, and the DLAN. However, given the

77 observational limitations, the DLAN was utilized to identify the mesosphere and
78 thermosphere via the ray-tracing theory. The objectives of this study were to (a) scrutinize
79 multi-layer CGW features produced by Super Typhoon Chaba (2016) from near the ground to
80 a height of 250 km, (b) to examine the entire propagation process of the CGWs excited by
81 typhoon from the lower atmosphere to the upper atmosphere, and (c) to provide new insights
82 into the coupling between different atmospheric layers.

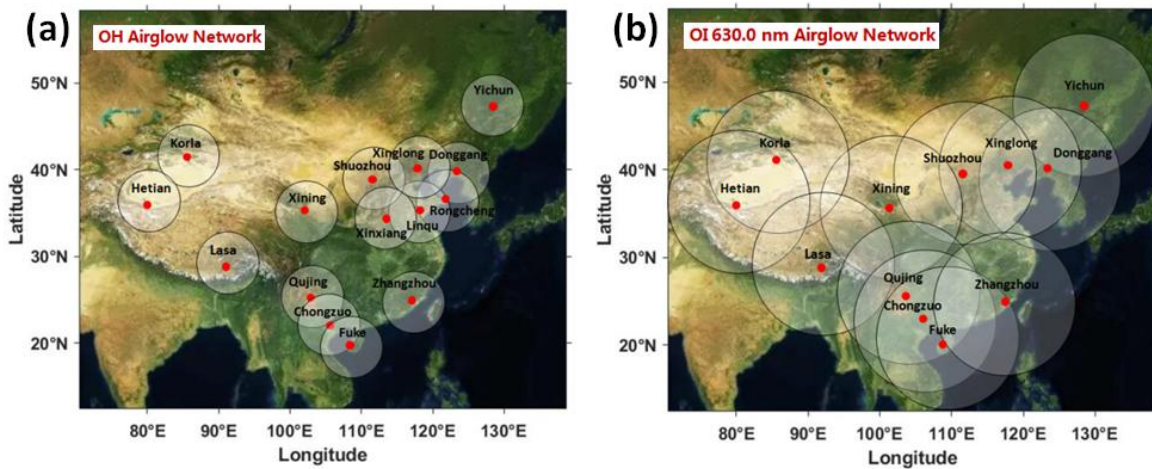
83 2. Data and Methods

84 2.1 Double layer all-sky airglow imager network data

85 ~~The~~ A DLAN, including an OH layer (~87 km) and ~~an~~ OI 630.0 nm layer (~250 km)
86 was established over ~~the~~ mainland China. The research aim of the DLAN is to explore the
87 physical mechanism of vertical and horizontal propagation, ~~as well as~~ and the evolution of
88 atmospheric waves, triggered by severe disasters, such as typhoons, earthquakes, and
89 tsunamis, in various middle and upper atmospheric layers. The OH airglow network
90 comprises 15 stations, including the first no-gap OH airglow all-sky imager network located
91 in northern China (Xu et al., 2015). The OI 630.0 nm airglow network contains 12 stations.
92 Each imager consists of a 1024×1024 pixel back-illuminated CCD detector and a Nikon16
93 mm/2.8D fish-eye lens with a 180° field of view (FOV). The OI 630.0 nm imager is operated
94 at the 3.0 nm band-width filter with a central ~~the centre~~ wavelength of 630.0 nm. Observations
95 using airglow optical remote sensing require only a few airglow imagers to cover a wide area,
96 although it is limited by meteorological conditions. Moreover, airglow observations can be
97 used to monitor multi-layer GW activities. Figure 1a and 1b illustrate the OH and OI 630.0
98 nm network station distribution maps, respectively, in China. The OI 630.0 nm network

99 covers nearly the entire mainland China. Furthermore, the DLAN provides an excellent
100 solution for studying the coupling process among different atmospheric layers, especially the
101 mesosphere and thermosphere.

102 Several standard procedures were applied to raw airglow images, including star
103 contamination subtraction, flat fielding to remove van Rhijin, and atmospheric extinction (Li
104 et al., 2011). The GW structure was retrieved by taking the deviation of each processed
105 image from a half-hour running average window image. Finally, the images were projected
106 onto the Earth's surface using the standard star map software and the altitude of the airglow
107 layer (Garcia et al., 1997). The altitudes of the OH and OI 630.0 nm emission layers were set
108 as approximately 87 km and 250 km, respectively.

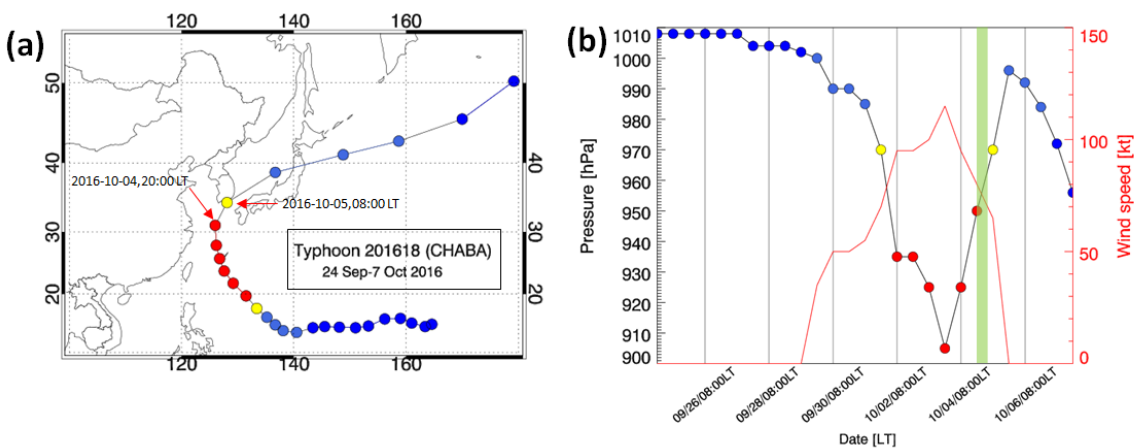


109 **Figure 1. (a)** OH airglow all-sky imager network (15 stations). **(b)** Red line (630 nm) airglow all-sky
110 imager network (12 stations). The circles on the maps give the effective observation ranges of OH and
111 Red line airglow imagers with diameters of about 800 km and 1800 km, respectively.
112

113 2.2 Development of Super Typhoon Chaba

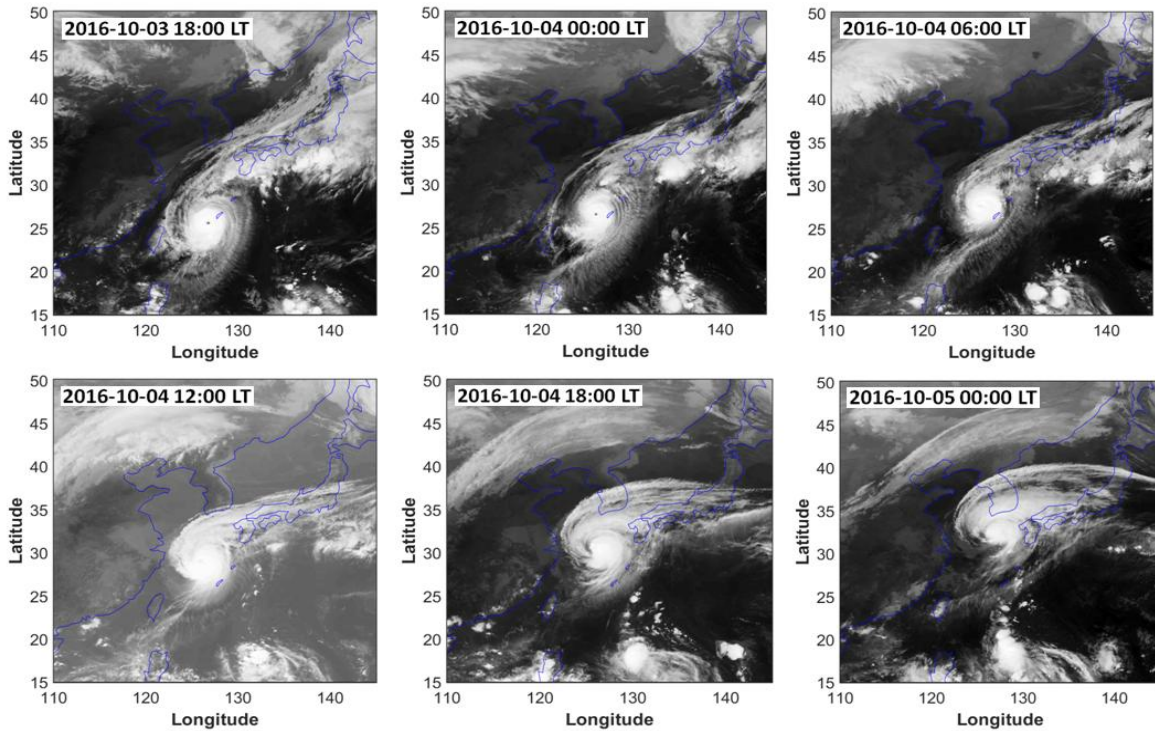
114 Super Typhoon Chaba (2016) developed in the north-western Pacific on 24 September
115 2016 and its track is shown in Fig. 2a. Initially, it moved westward and then turned
116 north-westward on 30 September. The central pressure in the eye of the typhoon and the

117 maximum wind speed are shown in Fig. 2b. On 3 October 2016 at ~~1220:00 UT~~1220:00 UTLT, the
 118 typhoon was in the mature stage with a minimum central pressure of 905 hPa and maximum
 119 sustained winds of approximately 59 m/s. The typhoon moved northward on ~~3-4~~3-4 October
 120 2016 at ~~1802:00 UT~~1802:00 UTLT until ~~4-5~~4-5 October 2016 at ~~1802:00 UT~~1802:00 UTLT. The typhoon continued
 121 moving towards the northeast and disappeared on ~~7-8~~7-8 October 2016 at ~~1802:00 UT~~1802:00 UTLT.
 122 Consecutive satellite images of the typhoon from MTSAT-1R from 18:00 LT on 3 October
 123 2016 to 00:00 LT on 5 October 2016 are shown in Fig. 3. MTSAT-1R, which belongs to the
 124 Japan Meteorological Agency, comprises a series of Geo-stationary Meteorological Satellites.
 125 MTSAT-1R is located at around 140 °E and covers East-Asia and the western Pacific region.
 126 The MTSAT-1R consists of four infrared channels (IR1, IR2, IR3, and IR4) and one visible
 127 channel (VIS). The MTSAT- IR1 was used in this study. The track of the typhoon was beyond
 128 the effective FOV of the OH network and at the edge of the effective FOV of the OI 630.0 nm
 129 network, which provides an excellent example for observing the CGWs stimulated by the
 130 typhoon and studying the coupling among the atmospheric layers.



131
 132 **Figure 2.** (a) The track of Typhoon Chaba is denoted by dots from 24 September to 7 October 2016 every
 133 12 hours. (b) Central pressure of Typhoon Chaba corresponding to the tracks in (a). The red line denotes
 134 the maximum sustained wind speed ~~is presented in red line~~. The green shadow band denotes marks the

135 time of ground-based airglow observation from 20:00 LT to 04:00 LT during the night of 4-5 October
136 2016.



137 **Figure 3.** Consecutive satellite images of the typhoon Chaba from MTSAT-1R. The ~~time span~~period is
138 from 18:00 LT on 3 October 2016 to 00:00 LT on 5 October 2016, with an interval of 6 hours.
139

140 2.3 ERA-5 reanalysis data

141 ERA-5 is a fifth-generation ECMWF atmospheric reanalysis that provides hourly data
142 for many atmospheric and wave parameters. ERA-5 is produced using a four-dimensional
143 variational data assimilation algorithm based on Integrated Forecast System (IFS), with 137
144 hybrid sigma/pressure (model) levels in the vertical from 1000 ~~hPa~~ to 0.01 hPa (0 ~~km~~ to 80
145 km). More details of the model, data assimilation system, and observation data used to
146 produce ERA-5 ~~have been~~ were described by Hersbach et al. (2020). Horizontal reanalysis
147 temperature and wind data with a pre-interpolated resolution of $0.25^\circ \times 0.25^\circ$ were used in this
148 study. ~~The horizontal resolution of the reanalysis temperature and wind data with a~~
149 ~~pre-interpolated resolution of $0.25^\circ \times 0.25^\circ$ was used in this study.~~

150 2.4 Ray tracing model

151 We used a ray-tracing method to estimate the source location of the thermospheric
152 secondary CGWs ~~We use a ray tracing method to track the excitation source of the~~
153 ~~thermosphere secondary CGWs. This~~ The model is was based on the a dispersion relation
154 that considers ~~the~~ molecular viscosity and thermal diffusivity (Vadas, 2007), as shown in
155 Equation (1):

$$156 \quad m^2 = \frac{k_H^2 N^2}{\omega_{Ir}^2 (1 + \delta_+ + \delta^2 / \text{Pr})} \left[1 + \frac{\nu^2}{4\omega_{Ir}^2} \left(k^2 - \frac{1}{4H^2} \right)^2 \frac{(1 - \text{Pr}^{-1})^2}{(1 + \delta_+ / 2)^2} \right]^{-1} - k_H^2 - \frac{1}{4H^2}, \quad (1)$$

157 where ω_{Ir} is the intrinsic frequency; $\mathbf{k}^2 = k_H^2 + m^2$, $k_H^2 = k^2 + l^2$; ~~k , l , and m are the zonal,~~
158 ~~meridional, and vertical wave number components of the GW, respectively. The horizontal~~
159 ~~wavelength (k_H) of the CGW was obtained from the ground-based airglow observations;~~
160 $N^2 = (g/T)(dT/dz + g/c_p)$ ~~is the square of the Brunt-Väisälä frequency, where g is the~~
161 ~~gravitational acceleration, T is the background temperature, c_p is the specific heat at constant~~
162 ~~pressure, respectively; H is the scale height; $\nu = \mu/\bar{\rho}$ is the kinematic viscosity, where μ is the~~
163 ~~molecular viscosity; and $\bar{\rho}$ is the background density; $\delta = \nu m/H\omega_{Ir}$, $\delta_+ = \delta(1 + \text{Pr}^{-1})$, where Pr~~
164 ~~is the Prandtl number. k , l , and m are the zonal, meridional, and vertical wave number~~
165 ~~components of the GW, respectively. The horizontal wavelength (k_H) of the CGW was~~
166 ~~obtained from the ground-based airglow observations; $N^2 = (g/T)(dT/dz + g/c_p)$ is the~~
167 ~~square of the Brunt-Väisälä frequency, where g is the gravitational acceleration, T is the~~
168 ~~background temperature, c_p is the specific heat at constant pressure, respectively; The~~
169 background temperature T and density $\bar{\rho}$ were obtained from the NRLMSISE-00 model
170 (Picone et al., 2002).

171 The group velocity of the wave packet is formalized by Equation (2):

$$172 \quad c_{gi} = dx_i/dt = \partial\omega/\partial k_i + V_i, \quad (2)$$

173 where $V_i(u, v, w)$ is the background wind, which was obtained from the Horizontal Wind

174 Model 14(Drob et al., 2015), and w is the vertical wind velocity, which was neglected. Using

175 Equations (1)-(2), we yield the ground-based (zonal, meridional, and vertical) group velocity

176 equation as follows (Vadas and Fritts, 2005):

$$177 \quad c_{gx} = \frac{k}{\omega_r B} \left[\frac{N^2(m^2 + 1/4H^2)}{(k^2 + 1/4H^2)^2} - \frac{v^2}{2} (1 - Pr^{-1})^2 \left(k^2 - \frac{1}{4H^2} \right) \frac{(1 + \delta_+ + \delta^2/Pr)}{(1 + \delta_+/2)^2} \right] + u, \quad (3)$$

$$178 \quad c_{gy} = \frac{l}{\omega_r B} \left[\frac{N^2(m^2 + 1/4H^2)}{(k^2 + 1/4H^2)^2} - \frac{v^2}{2} (1 - Pr^{-1})^2 \left(k^2 - \frac{1}{4H^2} \right) \frac{(1 + \delta_+ + \delta^2/Pr)}{(1 + \delta_+/2)^2} \right] + v, \quad (4)$$

$$179 \quad c_{gz} = \frac{1}{\omega_r B} \left\{ m \left[-\frac{k_H^2 N^2}{(k^2 + 1/4H^2)^2} - \frac{v^2}{2} (1 - Pr^{-1})^2 \left(k^2 - \frac{1}{4H^2} \right) \frac{(1 + \delta_+ + \delta^2/Pr)}{(1 + \delta_+/2)^2} \right. \right. \\ \left. \left. + \frac{v^4 (1 - Pr^{-1})^4}{16H^2 \omega_r^2} \frac{(k^2 - 1/4H^2)^2}{(1 + \delta_+/2)^3} - \frac{v^2}{Pr H^2} \right] - \frac{v_+ \omega_r}{2H} \right\}, \quad (5)$$

$$180 \quad \text{where } B = \left[1 + \frac{\delta_+}{2} + \frac{\delta^2 v^2}{16\omega_r^2} (1 - Pr^{-1})^4 \frac{(k^2 - 1/4H^2)^2}{(1 + \delta_+/2)^3} \right], v_+ = v(1 + Pr^{-1}).$$

181 3. Results

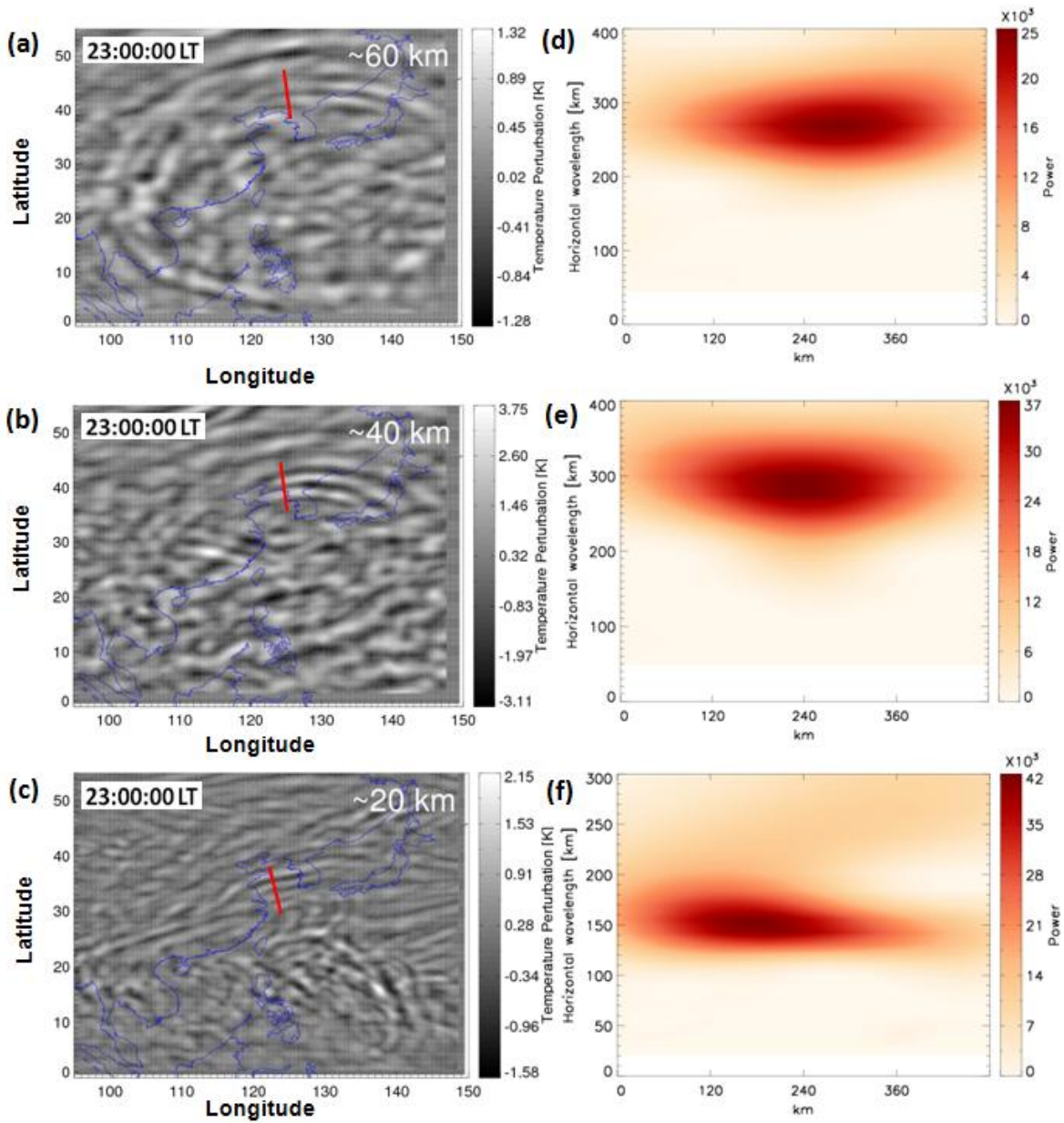
182 ~~CGWs were observed in OH and the OI 630.0 nm airglow networks during 2-5 October~~
 183 ~~and 3-4 October, respectively, during super Typhoon Chaba (2016). This study focused on the~~
 184 ~~CGW event that occurred on 4 October.~~

185 3.1 Propagation of typhoon-induced CGWs in the stratosphere

186 We extracted the CGWs excited by Typhoon in the stratosphere from the ERA-5
 187 reanalysis data. Figure 4a, 4b, and 4c show the multilayer temperature perturbations at
 188 approximately 60 km at 24:00LT, 40 km, and 20 km at 23:00 LT, retrieved from the ERA-5

189 reanalysis on 4 October 2016, respectively. Temperature perturbations were calculated by
190 subtracting the background with a 7×7 grid point running mean at 20 km and 17×17 grid
191 point running mean at 40 km and 60 km. We found that the temperature disturbance was
192 about ± 1.5 -2 K at 20 km and ± 3 -4 K at 40 km. Using the ECMWF reanalysis data, Kim
193 et al. (2009) reported a similar temperature disturbance (± 4 K) at 40 km altitude. Becker et al.
194 (2022) showed that typical temperature perturbation amplitudes simulated by a High
195 Altitude Mechanistic general Circulation Model were ± 1 -2 K in the wintertime lower
196 stratosphere and ± 5 K in the stratopause region. However, the temperature disturbance at 60
197 km altitude was only ± 1.3 K and did not increase with increasing altitude, which may be
198 caused by this altitude being well within the sponge layer of the reanalysis model. Figure 4d,
199 4e, and 4f show the corresponding wavelet analysis contours of the red line in Fig. 4a, 4b,
200 and 4c. ~~The temperature perturbations were calculated by subtracting the background from a~~
201 ~~5×5 grid point running mean.~~ The expansion area of CGW at the height of 20 km (Fig. 4c)
202 was small, and the horizontal wavelength ~~is~~ was approximately 150 km from Fig. 4f. Liu et al.
203 (2014) utilized the Whole Atmosphere Community Climate model and showed that the
204 horizontal area of the CGW expansion increases with increasing ~~an increase in~~ altitude. The
205 CGWs were present over ~~embraced~~ a large area of ~~(0° N -50° N)~~ and ~~(100° E -150° E)~~ at
206 approximately 60 km. The distance of the CGWs, extending from the center of the circle
207 ranged from 500 km (at approximately 20 km height) to 3000 km (at approximately 60 km
208 height). The ERA-5 reanalysis data was utilized for characterizing the scale of the CGWs and
209 indicated no small-scale fluctuation. According to the wavelet analysis of Fig. 4d and 4e, the
210 horizontal wavelength_s of the northward propagating CGW at 60 km (Fig. 4a) and 40 km

211 (Fig. 4b) ~~is~~ were approximately 265 km and 290 km, respectively.



212

213 **Figure 4.** Temperature perturbations at (a) ~60 km ~~at 24:00LT~~, (b) ~40 km, and (c) ~20 km at 23:00LT
214 on 4 October 2016 derived from ERA-5 reanalysis. (d) ~~The w~~Wavelet power spectrum along the red line
215 in (a), (e) ~~the~~ wavelet power spectrum along the red line in (b), and (f) ~~the~~ wavelet power spectrum along
216 the red line in (c).

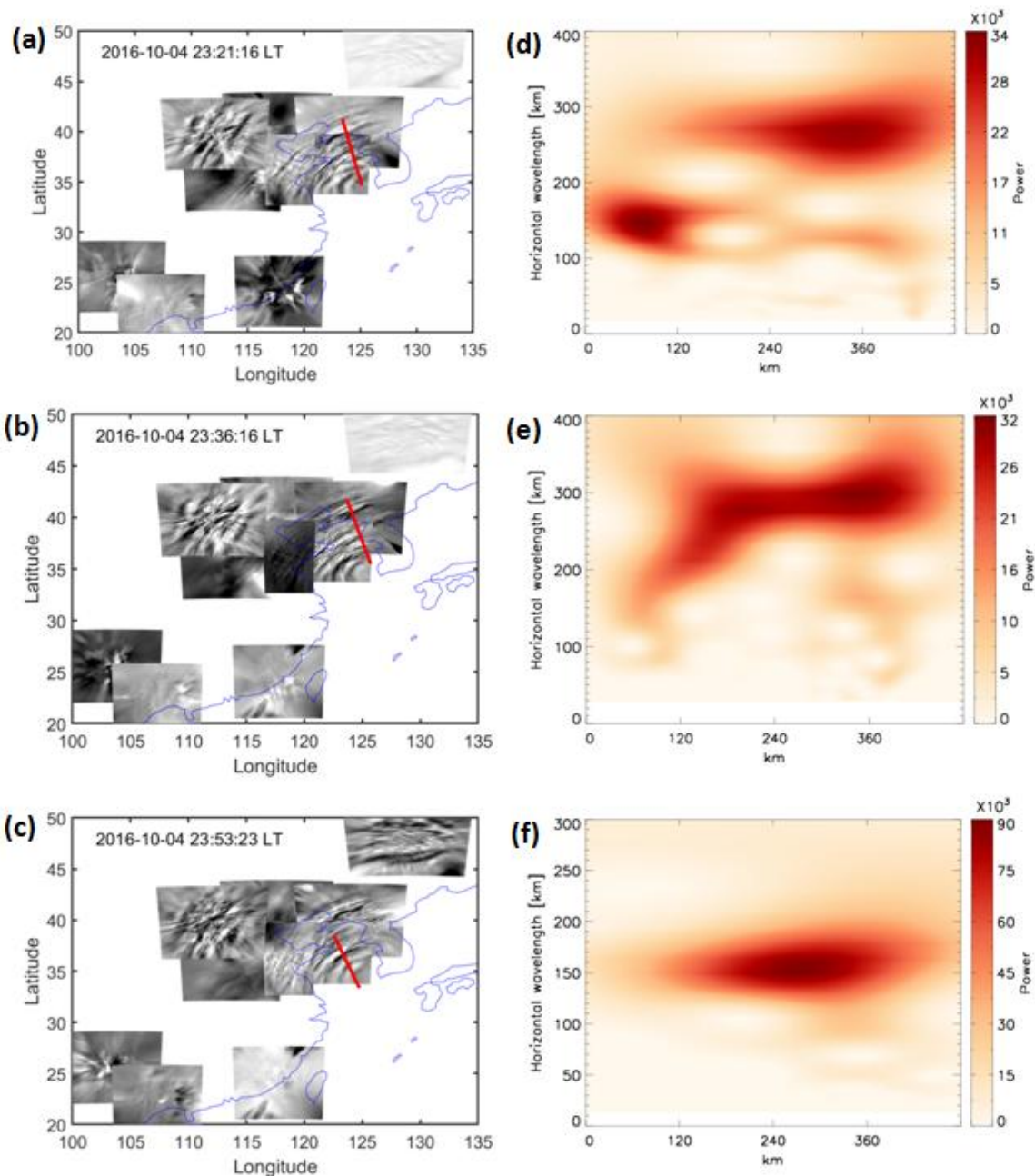
217 3.2 Propagation of typhoon-induced CGWs in the mesosphere

218 As the typhoon moved along the coast of China, CGWs were identified at ten stations

219 in the OH network. Animation 1 shows that CGWs were observed by the OH airglow
220 network during 20:00–04:00 LT (the detailed data can be downloaded from the
221 Supplementary Material). As the weather conditions in North China during the study period
222 were better than those in South China, we identified clearer wave structures at the northern
223 stations ~~compared to those~~ than at the southern stations. Nevertheless, circular wave
224 structures were visible for brief clear weather intervals at the Zhangzhou, Qujing, and
225 Chongzuo stations. The CGWs in the mesopause region extended to 2500 km, thereby
226 nearly covering the effective FOV of the OH airglow network.

227 ~~Although the time resolution of the ERA-5 reanalysis data is only 1 h, we can use the~~
228 ~~OH airglow network with a high spatial (1 km) and temporal resolution (1 min) to track the~~
229 ~~CGWs at different altitudes through the reanalysis data. As long as the CGWs do not~~
230 ~~encounter the critical layer or break, the phase plane of CGWs from ERA-5 reanalysis~~
231 ~~datasets can propagate to the OH airglow layer. Through the propagation group velocity, we~~
232 ~~can determine the propagation time to the OH layer. Compared with the~~ A single dominant
233 horizontal wavelength is seen at the altitudes of 20 km, 40 km, and 60 km in the ERA-5
234 reanalysis due to the limited resolution. In contrast, the horizontal scales of the CGW
235 obtained by the OH airglow network were diverse, ranging from approximately 30 km to
236 300 km as the imager has much higher spatial resolution. A single dominant horizontal
237 ~~wavelength of CGW at the altitude of 20km, 40km, and 60km obtained by the~~
238 ~~ERA-5 reanalysis due to the limitation of resolution. In contrast the horizontal scales of CGW~~
239 ~~obtained by OH airglow network are diverse, ranging from approximately 30km to 300km.~~
240 More importantly, we found some CGWs in the OH airglow layer, which ~~are~~ were close to

241 the CGW wavelengths at 20 km, 40 km, and 60 km altitudes. ~~To verify whether the phase~~
242 ~~plane of the same wave was propagated from the reanalysis data layer to the OH layer, In~~
243 ~~order to verify whether it is the same event,~~ we used the group velocity to estimate the time
244 when the phase plane of CGW at the altitudes of 20 km, 40 km, and 60 km ~~reaches-reached~~
245 the OH airglow layer. The times required for the CGW in the three-layer disturbance
246 diagram in Fig. 4a, 4b, and 4c ~~to reaching the~~ OH layer were approximately ~~18~~ 21 minutes,
247 36 minutes, and 53 minutes. Therefore, the time when the phase plane of CGWs from
248 ERA-5 at the height of 60 km, 40 km, and 20 km reaches the OH airglow layer is
249 approximately ~~0023:18~~23:21 LT, 23:36 LT, and 23:53 LT as shown in Fig. 5a, 5b, and 5c,
250 respectively. ~~The wavelet analysis of Fig. 5f showed We find~~ that the horizontal wavelength
251 of CGW in the OH airglow layer (Fig. 5c) is approximately 156 km ~~from the wavelet~~
252 ~~analysis of Fig. 5f,~~ the observed ~~observation~~ period is approximately 23 min, and the
253 horizontal speed is approximately 113 m/s, which is similar to the dominant horizontal
254 wavelength of the CGWs in the ERA-5 reanalysis ~~horizontal wavelength of the atmosphere~~
255 at ~~a height of~~ 20 km altitude. Similarly, the horizontal wavelengths of CGW in the OH
256 airglow layers (Fig. 5a and 5b) ~~is-were~~ approximately 270 km and 295 km from the wavelet
257 analysis of Fig. 5d and 5e, ~~the observation period is approximately 36 min, and the~~
258 ~~observation horizontal speed is approximately 137 m/s,~~ which is similar to the dominant
259 horizontal wavelength of the CGWs in the ERA-5 reanalysis ~~horizontal wavelength of the~~
260 ~~atmosphere~~ at ~~the height of~~ 60 km and 40 km altitudes. This suggests that the same CGW
261 event can be perfectly tracked at different layer altitudes, ~~and it also suggests~~ that the CGWs
262 in the mesosphere come from the direct excitation of the typhoon.



263

264 **Figure 5.** OH airglow emission perturbations induced by CGWs observed by the OH airglow imager
 265 network at (a) 23:18-21 LT, (b) 23:36 LT, and (c) 23:53 LT on 4 October 2016. (d) The wavelet
 266 power spectrum along the red line in (a), (e) the wavelet power spectrum along the red line in (b), and (f)
 267 the wavelet power spectrum along the red line in (c).

268 **3.3 How does typhoon-induced CGWs propagate to the thermosphere?**

269 Furthermore, the OI 630.0nm airglow imager network observations at the Donggang
 270 station revealed that the partial concentric ring feature lasted for 1 h from approximately

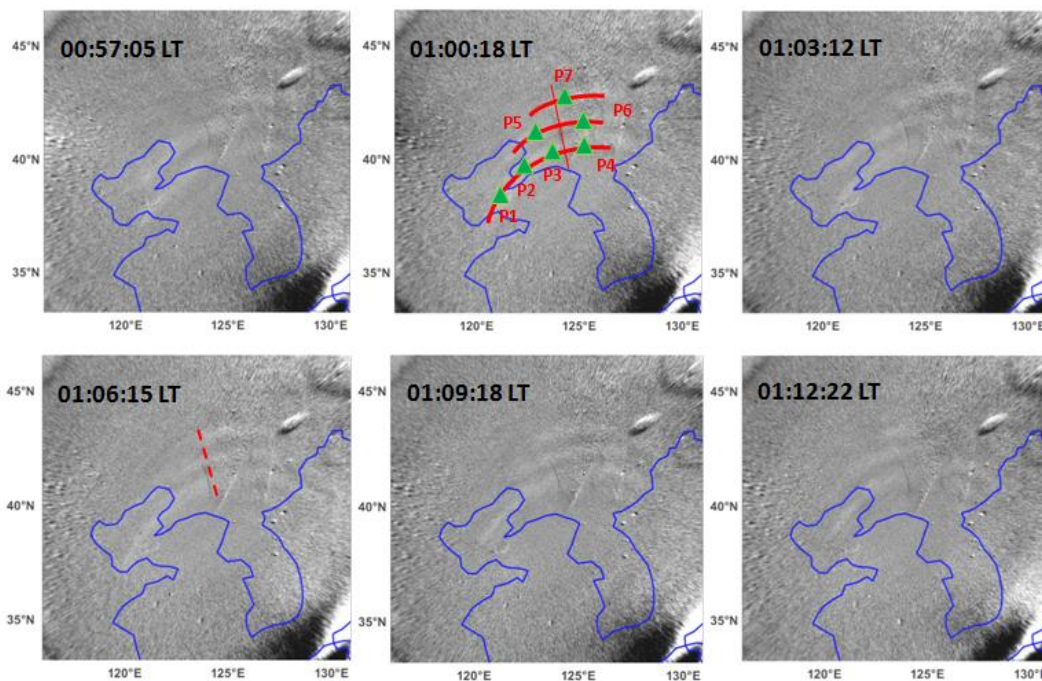
271 ~~00:30 LT to 01:30 LT. The GWs generated in the troposphere can enter the thermosphere~~
272 ~~before breaking and/or dissipating (Vadas, 2007; Azeem et al., 2015). In contrast,~~
273 ~~thermospheric GWs can originate from secondary waves generated by the breaking of GWs in~~
274 ~~the mesosphere (Vadas and Fritts, 2003; Vadas and Crowley, 2010; Vadas and Azeem, 2021).~~

275 Figure 6 shows the time sequence of the OI 630.0 nm airglow images from 00:57:05 LT
276 to 01:12:22 LT on the night of 4 October 2016. Three curved phase fronts are clearly visible.

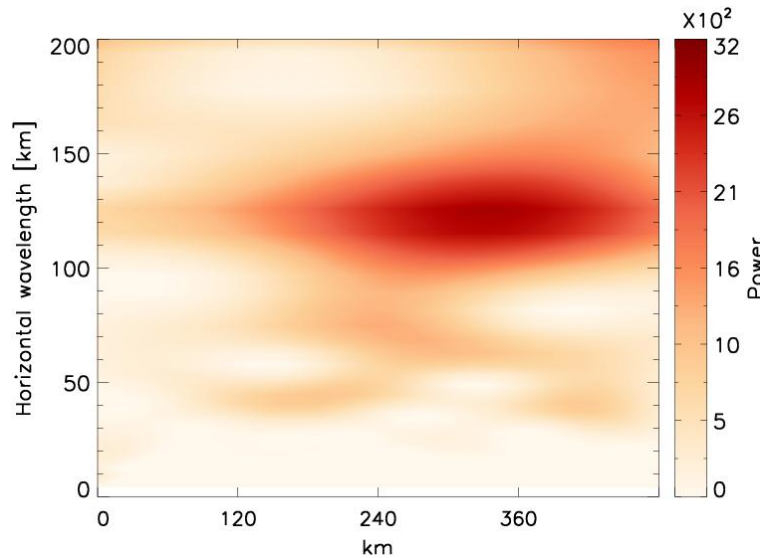
277 ~~The wave packet observed in the OI 630 nm airglow was quasi-monochromatic. The wave~~
278 ~~scale observed at the OI 630.0 nm airglow was monochromatic. According to the wavelet~~
279 ~~analysis spectrum in Fig. 7, the horizontal wavelength was approximately 120 km. The~~
280 ~~observation period and phase velocity were 10 min and 200 m/s, respectively. It has a~~
281 ~~horizontal wavelength of approximately 120 km, observed period of approximately 10 min,~~
282 ~~and observed phase speed of approximately 200 m/s. The horizontal wavelength is was~~

283 somewhat less than the multi-scale typhoon-induced concentric traveling ionosphere
284 disturbances with a horizontal wavelength from 160 to 200 km in the GNSS-TEC network
285 as reported by Chou et al. (2017). ~~We superimposed the thermospheric CGWs on the OH~~
286 ~~airglow observation images denoted by the blue arcs in Fig. 9. The solid circles represent the~~
287 ~~approximate fit of CGWs, as observed by the OH airglow network. The centre of the circles~~
288 ~~is located at (31°N, 127°E), and is marked by a red dot. Compared with the single-scale~~
289 ~~wave observed in the OI 630.0 nm layer, multi-scale CGWs are visible from OH network~~
290 ~~observations (see Fig. 9). The CGW observed in the OI 630.0 nm airglow having had much~~
291 ~~faster phase speed and shorter period, which indicate that its propagation trajectory was~~
292 ~~relatively vertical. Nevertheless, the waves with a scale similar to that of the thermosphere~~

293 ~~GWswere not identified by the OH airglow network. This means that they will not propagate~~
 294 ~~as far horizontally as the CGWs noted as dominant in the OH layer. Moreover~~ Indeed,
 295 compared with the long-distance extension of the CGWs in the mesosphere, the propagation
 296 distance of the CGWs in the thermosphere was only 600 km. ~~Moreover,~~ Numerical
 297 simulations revealed that the thermosphere GWs may originate from secondary GWs
 298 generated by the breaking of primary GWs in the mesosphere or thermosphere region (Vadas
 299 and Crowley, 2010). We argue that the following phenomenon can represent the potential
 300 driver of this pattern. Specifically, the thermospheric CGW observed by the OI 630.0 nm
 301 airglow imager was not directly generated by the typhoon, but a secondary GW. To test this
 302 hypothesis, ~~the~~ backward ray-tracing analysis was applied. In this way, we determined the
 303 source of the CGW observed in the thermosphere.



304
 305 **Figure 6.** A time sequence of OI 630.0 nm airglow emission perturbation images observed by Donggng
 306 station during 00:57:05 - 01:12:22 LT on the night of 4 October 2016. Green triangles (P1-P7) in the red
 307 arcs are used as ray tracing sampling points. The blue line in each panel represents the coastline.



308

309 **Figure 7. Wavelet power spectrum along the red line at 01:00:18 LT in Fig. 6.**

310 We sampled ~~four~~ seven points (green triangles) on a circular wavefront (red line in Fig.

311 6) at 01:00:18 LT as the starting point for backward ray tracing. The starting height of the

312 backward ray tracing was 250 km. The profile of the winds used in the ray tracing is shown

313 in Fig. 8a. The ray tracing trajectories of the ~~four~~ seven sampling points are shown in Fig. 8b.

314 We used the following criterion to terminate the ray tracing ~~that~~: the square of the vertical

315 wavenumber should be negative. The ray-tracing results of three different heights of 240 km,

316 250 km, and 260 km were analyzed. The maximum uncertainty of horizontal change of

317 ray-tracing termination point caused by different starting heights was approximately $\pm 0.36^\circ$

318 in latitude and $\pm 0.17^\circ$ in longitude (see Figure 8c). Subsequently, ~~four~~ seven backward

319 traced trajectories took 37 minutes and terminated at ~~the an~~ altitude of approximately 95 km

320 thereby indicating that it met the reflection layer ~~37 min earlier~~. which, according to linear

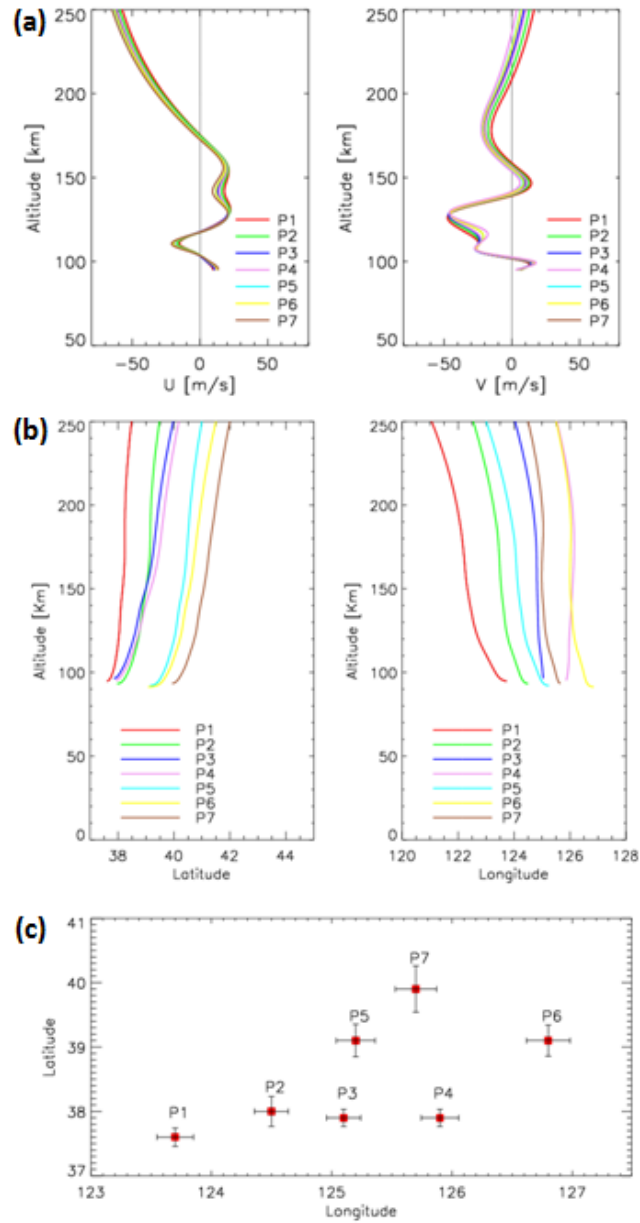
321 theory, suggests that the thermospheric CGW could not have come from below 95 km

322 according to linear theory. The thermospheric CGW could have been generated at any

323 altitude between 95 km and the altitude of the OI 630.0 nm airglow. In other words, the

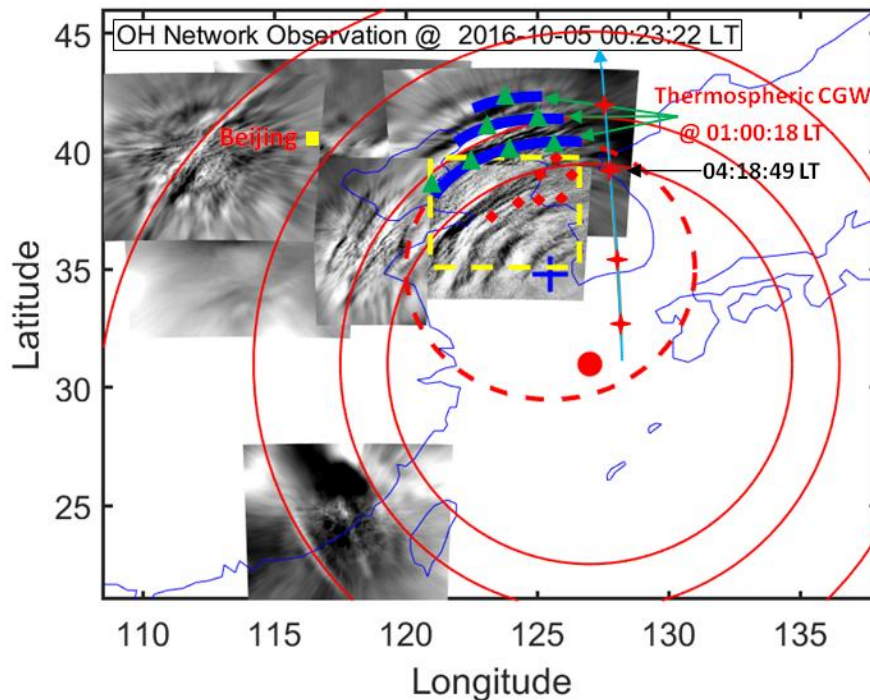
324 CGW observed in the thermosphere was excited ~~after at~~ approximately 00:23 LT.
325 Meanwhile, Figure ~~7e-9~~ presents the CGWs observed by the OH airglow network at
326 00:23:22 LT. We superimposed the thermospheric CGWs along with the starting ray tracing
327 points (green triangles) reproduced from Fig. 6, and the backward ray tracing termination
328 points (red diamonds) on the OH airglow observation images. The dotted circle represents
329 the approximate fitting thermospheric CGW fronts. The center of the circle is marked by a
330 blue cross. Compared with the single-scale wave observed in the OI 630.0 nm layer,
331 multi-scale CGWs were visible from OH network observations. We ~~find~~ found that the
332 termination points of ray tracing almost ~~fall~~ fell above the mesopause region, which showing
333 clear signs of dissipation and/or nonlinear processes. This suggests that the CGW observed
334 in the thermosphere did not directly originate from the typhoon, but may have emerged due
335 to the dissipation and/or nonlinear processes of typhoon-induced CGW in the mesopause
336 region. However, the backward tracing terminal positions (red diamonds in Fig. 9) did not
337 coincide with the fitting circle center position (blue cross in Fig. 9). Nevertheless, according
338 to numerical simulation work by Vadas et al. (2009), large winds can shift the apparent
339 center of concentric rings from the location of the convective plume. Indeed, we found
340 strong southward winds from 100 km to 140 km (with a peak value of 50 m/s at 150 km
341 altitude) and from 160 km to 220 km (with a peak value of 25 m/s at 175 km altitude)
342 altitudes (right panel of Figure 8a). So the center of the thermospheric CGW can be shifted
343 southward from the location of the thermospheric CGW sources in the mesopause region.
344 For the zonal wind, the westward wind dominated from the upper mesosphere to the
345 thermosphere (left panel of Figure 8a). Similarly, the thermospheric CGW center position

346 shifted westward. Therefore, the assumed center (blue cross) of the partial concentric ring
347 GWs (blue arcs) actually shifted to the southwest from the real source location , which can
348 explain why the ray-tracing result for the assumed GW source did not match the fitting
349 center of the partial concentric ring thermospheric GWs. As the ray_tracing model used in
350 this study ~~depends~~depended on the linear theory and ~~does~~did not consider the wave-wave
351 and wave-mean flow interactions and tunneling, the ray tracing results ~~are~~were limited and
352 should be ~~carefully~~ taken into consideration carefully.



353

354 **Figure 78.** (a) Wind profiles along the seven ray-tracing paths. (b) Ray paths of the wave starting from the
 355 seven sampling points in Fig. 6. (c) Horizontal area distribution of the terminal positions of the seven
 356 backward traced trajectories. Error bars give standard deviation for each point from the starting altitude of
 357 240 km, 250 km, and 260 km.



358

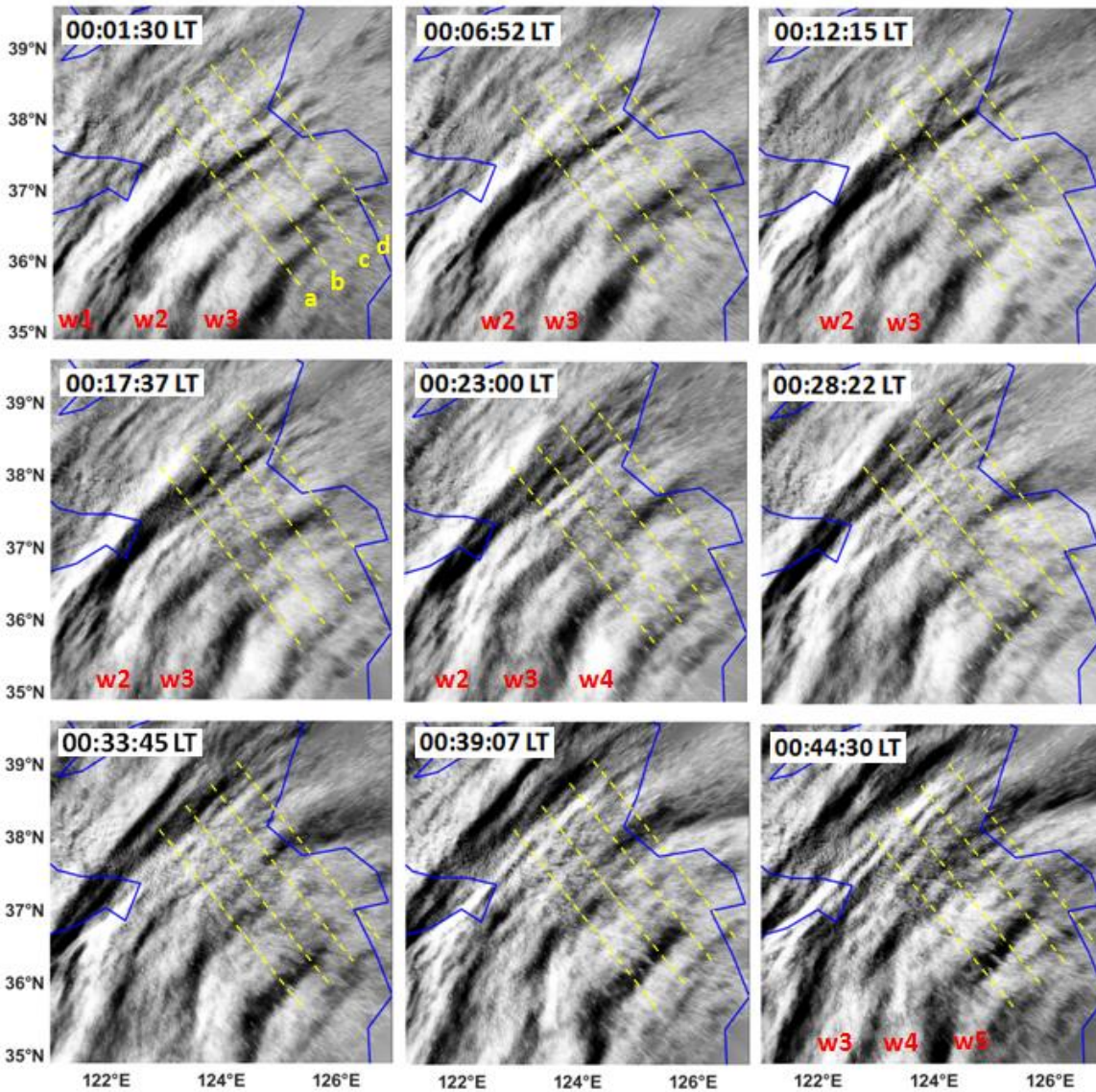
359 **Figure 9.** ~~Two~~ Double layer CGW superimposed graph: The blue arcs represent the thermospheric CGW
 360 observed at 01:00:18 LT. The dotted circle represents the approximate fitting blue arcs. The blue cross
 361 marks ~~The~~ ~~the~~ center of the circle ~~is marked by a blue cross~~. The solid circles represent the approximate
 362 fitting CGWs observed by the OH airglow network. The red dot marks the center of the circles ~~is marked~~
 363 ~~by a red dot~~. The green triangles and red solid diamonds lines represent the trace start and termination
 364 points ~~and backward trajectories~~, respectively. The red crosses represent the sounding footprints of the
 365 TIMED/SABER measurements. The yellow box marks the location of the meteor radar station.

366

367 4. Discussion

368 ~~We showed that the strong CGWs and wave dissipating events were observed by the~~
 369 ~~OH airglow network both before and during the observed thermospheric CGWs on 4~~
 370 ~~October 2016.~~ Figure 8-10 presents a time sequence of OH airglow images in the range
 371 marked by the yellow dotted rectangle in Fig. ~~7e~~ 9. The images were retrieved from the
 372 Rongcheng station from 00:01:30 to 00:44:30 LT on the night of 4 October 2016. At
 373 00:01:30 LT, three distinct curved wavefronts with the horizontal wavelengths of

374 approximately 96 km were identified. Interestingly, ~~the~~ wavefronts 2 and 3 collided and
 375 connected in the northeast, indicating that wave-wave nonlinear interactions may have
 376 occurred.

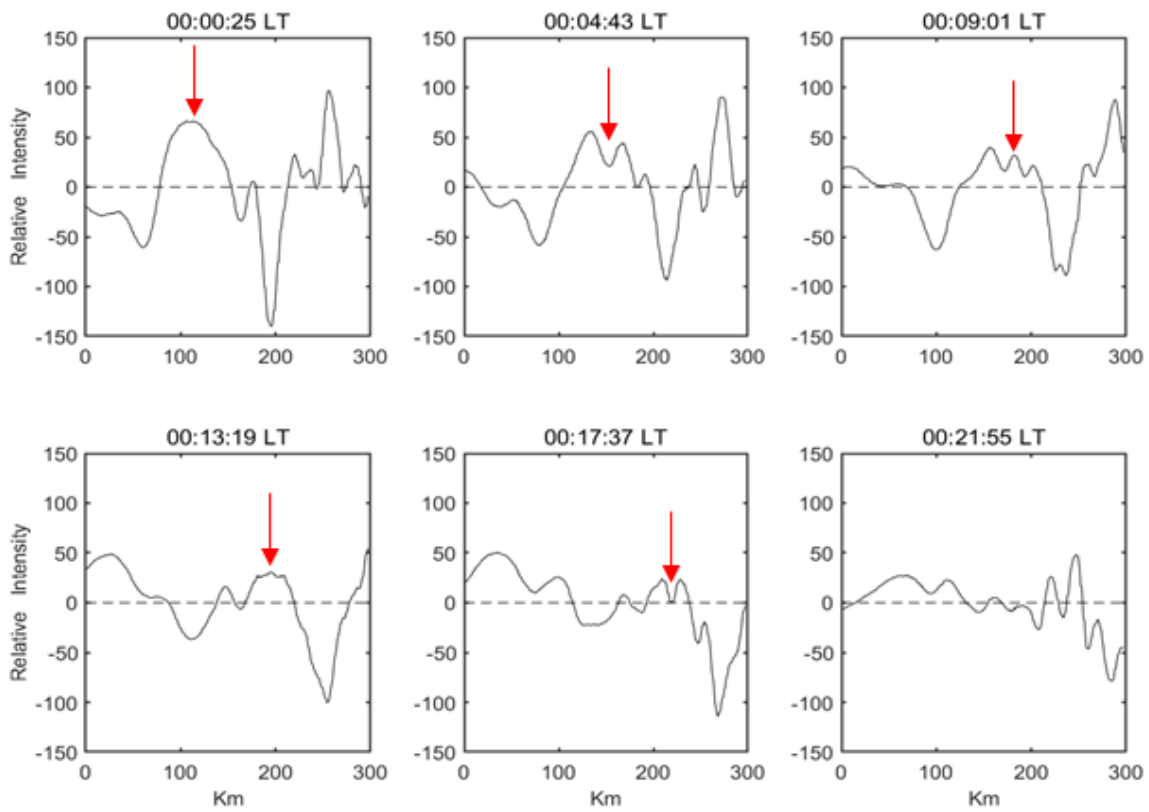


377
 378 **Figure 810.** A–T Time sequence of OH airglow emission perturbation images observed by Rongcheng
 379 station during 01:01:30–00:44:30 LT on the night of 4 October 2016. w1–w5 denote the wavefronts of the
 380 CGW. ~~Red squares denote the terminal positions of the four backward traced trajectories in Fig. 7a.~~ The
 381 blue line in each panel represents the coastline.

382 We elucidated the dissipation process of the CGW_s in detail by examining the

383 evolution process of ~~its~~their amplitude. Figure ~~9-11~~ shows the time series of the OH image
384 slices perpendicular to the wavefronts. A dominant wavelength of approximately 150 km
385 can be confirmed. As a result, we found a significant attenuation of the amplitude from
386 00:06:52 LT to 00:~~21~~17:55-37 LT. At 00:06:52 LT, while the relative average power ~~is~~was
387 2.3×10^3 , and the amplitude decreased gradually with time. At 00:~~21~~17:55-37 LT, the
388 average power decreased to $0.140.15 \times 10^3$. ~~At the same time, w~~We also identified the
389 generation of approximately 110 km and 20-50 km small-scale waves from the larger scales,
390 which may be caused by wave-wave nonlinear interactions and/or wave breaking. We
391 overlayed the OI 630 nm airglow relative intensity variation on the OH airglow variation
392 and Figure 12 shows OH and OI 630 nm airglow relative intensity variations. The OH plot
393 was obtained at 00:29:27 LT and the OI 630 nm plot at 01:06:15 LT. The time interval of 37
394 min was calculated by the above ray tracing analysis. We obtained similar scale fluctuations
395 were obtained in the two airglow layers. The horizontal wavelength of the wave obtained by
396 the OI 630 nm airglow layer was approximately 118 km. The OH airglow layer has also
397 obtained near-scale fluctuations with wavelengths of approximately 109 km. Therefore, the
398 CGW in the thermosphere may come from breaking or nonlinear processes of that primary
399 gravity waves.

400



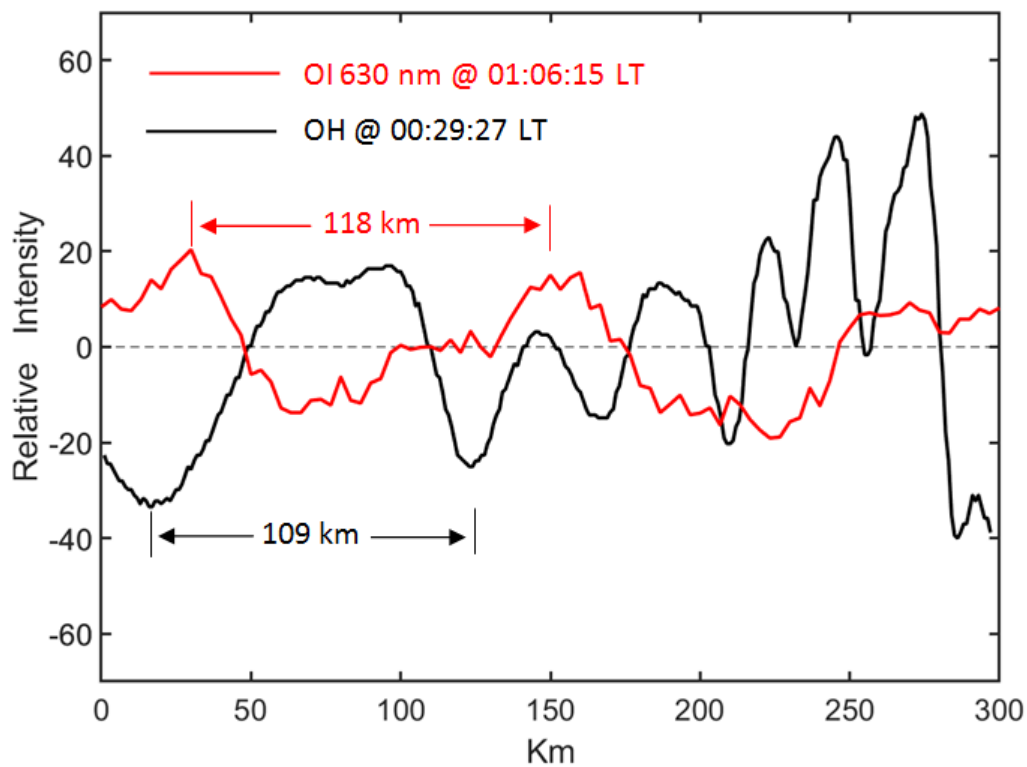
401

402

403

404

Figure 11. Time series of averaged OH image slices perpendicular to the wavefronts as marked by four yellow dotted lines (a, b, c, and d) in Fig.10. The wavefronts propagate from left to right. The red arrows mark the evolution of the wavefront peak.



405

406 Figure 12. OH (black) and OI 630 nm (red) airglow relative intensity variations. The OH relative
 407 intensity variation is obtained as in Fig. 11. The OI 630 nm relative intensity variation is from the red
 408 dotted line in Fig.10 at 01:06:15 LT.

409

410 However, wavepacket amplitude fluctuations can also result from the transient nature

411 of the wavepacket. However, the observed CGW dissipation may be caused by the upward

412 CGW passing through the airglow. Notably, the observed CGW dissipation is real, unless it

413 propagates horizontally. The propagation state can be studied by using the dispersion

414 relationship with GW, but the dissipation region of the CGW lacks the real-time background

415 temperature and wind field. In this context, TIMED/SABER can be beneficial because it

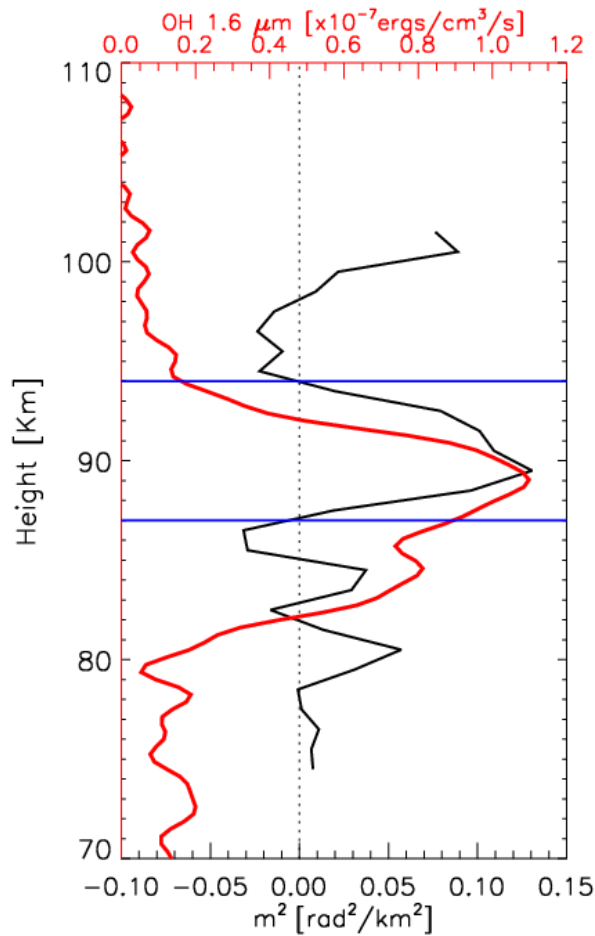
416 occurred near the wave-dissipation region; however, the time lag was close to approximately

417 4 h. On this basis, we used the meteor radar wind field data from the Beijing station as

418 auxiliary information. We further examined the dispersion relationship of GW, thereby

419 shedding some light on the possible propagation state of dissipative waves. Figure 1013

419 presents the vertical wave number m^2 profile derived from the Beijing meteor radar wind
420 and the temperature from the TIMED/SABER sound at 04:18:49 LT, as marked in Fig.7e9.
421 The wave parameters used were from the wavefronts (w1-w5) in Fig.10. The average
422 horizontal wavelength was approximately 96 km and the average observed phase velocity is
423 approximately 90 m/s. We identified a clear duct (from 87 km to 94 km) near the peak of the
424 OH airglow layer. Note that the duct can control the horizontal propagation of CGW. This
425 implies that the CGW may indeed be dissipated. In contrast, the upper boundary of the duct
426 ~~coincides~~ coincided with the height of the ray-tracing termination area mentioned above.
427 During ~~the~~ wave dissipation, momentum deposition occurs in the background atmosphere
428 and can produce bodyforces that stimulate ~~the~~ secondary GWs (Fritts et al., 2006; Chun and
429 Kim, 2008; Smith et al., 2013; Vadas et al., 2018; Heale et al., 2020). In addition, the
430 secondary waves can be generated by momentum transferred nonlinearly from the primary
431 wave mode to harmonics or subharmonics (Snively, 2017). Local momentum flux
432 divergence associated with wave breaking, vortex generation, and wave interactions can also
433 generate secondary GWs (Fritts et al., 2006).
434



435

436 **Figure 1013.** Vertical wave number m^2 derived from the temperature from TIMED/SABER sound at
 437 04:18:49 LT and the meteor radar wind from Beijing station marked in Fig. 7e9. The red line represents
 438 the OH1.6 μm emission intensity obtained by the TIMED/SABER. The horizontal lines represent the top
 439 and bottom boundaries of the duct region.

440

441 5. Summary

442 In this study, a ~~double layer airglow network (DLAN)~~ was used to capture ~~the~~ CGWs
 443 over China, ~~which that~~ were excited by the Super Typhoon Chaba (2016). ~~When As Super~~
 444 Typhoon Chaba (2016) moved northward along the coast of the Chinese Mainland and
 445 developed to a mature stage, remarkable multi-layer CGW features produced by the
 446 Typhoon from near the ground to a height of 250 km were observed by ERA-5 reanalysis and

447 airglow network. We applied the MTSAT-1R observations, ERA-5 reanalysis data, and
448 backward ray tracing and to quantitatively described the physical mechanism of
449 typhoon-generated CGWs propagating throughout the stratosphere, mesosphere, and
450 thermosphere.

451 The temperature disturbance was approximately ± 1.5 -2 K at 20 km and ± 3 -4K at 40
452 km. However, the temperature disturbance (± 1.3 K) at 60 km altitude did not increase with
453 further increase in altitude, which may be caused by the sponge layer effect. Using
454 reanalysis of multi-layer temperature disturbance, group velocity of gravity wave and
455 wavelet analysis, we demonstrated that the CGWs in the mesopause region were excited
456 directly by the typhoon.

457 Due to the observational limitations, a backward ray-tracing theory was used to connect
458 the upper mesosphere and GWs to the thermosphere. We found that the termination points of
459 ray tracing of the thermospheric CGW almost fell above the mesopause region, which shows
460 clear signs of primary CGW dissipation and/or nonlinear processes. Backward ray-tracing
461 analysis and the CGWs evolution process observed by OH network suggested that the CGW
462 observed in the thermosphere did not directly originate from the typhoon but may have
463 emerged due to dissipation and/or nonlinear processes of typhoon-induced CGWs in the
464 mesopause region. Airglow network observations combined with numerical simulation to
465 study the generation of secondary wave in detail will be carried out in the future.

466
467
468
469

470 ***Data availability***

471 The Double Layer Airglow Network data are available at <http://159.226.22.74/>. The ERA-5
472 reanalysis data are downloaded from the Copernicus Climate Change Service Climate Data
473 Store through <https://www.ecmwf.int/en/forecasts/datasets/reanalysis-datasets/era5>. The
474 typhoon information are provided at <http://agora.ex.nii.ac.jp/digital-typhoon/>. MTSAT-1R
475 data is accessed from <http://webgms.iis.u-tokyo.ac.jp/>.

476

477 ***Video supplement***

478 A video of detailed evolutions of CGWs excited by the Typhoon observed by OH airglow
479 observation network is provided (<https://doi.org/10.5446/55348>).

480

481 ***Author contributions***

482 J. X conceived the idea of the manuscript. Q. L. carried out the data analysis, interpretation
483 and manuscript preparation. H. L. L., X. L and W. Y. contributed to the data interpretation
484 and manuscript preparation. All authors discussed the results and commented on the
485 manuscript.

486

487 ***Competing interests***

488 The authors declare no competing interests.

489

490 ***Acknowledgements***

491 This work was supported by the National Science Foundation of China (41974179 and

492 41831073), Pandeng Program of National Space Science Center, Chinese Academy of
493 Sciences and the Strategic Priority Research Program of Chinese Academy of Sciences
494 (XDA17010301), and the Informatization Plan of Chinese Academy of Sciences
495 (CAS-WX2021PY-0101). The work was also supported by the Specialized Research Fund
496 for State Key Laboratories. We acknowledge the use of data from the Chinese Meridian
497 Project.

498

499 **References**

500 Azeem, I., Yue, J., Hoffmann, L., Miller, S. D., Straka, W. C., and Crowley, G.: Multisensor
501 profiling of a concentric gravity wave event propagating from the troposphere to the
502 ionosphere, *Geophys. Res. Lett.*, 42, 7874–7880, 2015.

503 [Becker, E., Vadas, S. L., Bossert, K., Harvey, V. L., Zülicke, C., and Hoffmann, L.: A](#)
504 [High-resolution whole atmosphere model with resolved gravity waves and specified](#)
505 [large-scale dynamics in the troposphere and stratosphere, *Journal of Geophysical*](#)
506 [Research: Atmospheres, 127, 2022.](#)

507 [Chun, H.-Y., and Kim, Y.-H.: Secondary waves generated by breaking of convective gravity](#)
508 [waves in the mesosphere and their influence in the wave momentum flux, *J. Geophys.*](#)
509 [Res., 113, D23107, 2008.](#)

510 Chou, M. Y., Lin, C. C. H., Yue, J., Tsai, H. F., Sun, Y. Y., Liu, J. Y., and Chen, C. H.:
511 Concentric traveling ionosphere disturbances triggered by Super Typhoon Meranti
512 (2016), *Geophys. Res. Lett.*, 44, 1219–1226, 2017.

513 Dong, W., Fritts, D. C., Lund, T. S., Wieland, S. A., and Zhang, S.: Self - acceleration and

514 instability of gravity wave packets: 2.two - dimensional packet propagation, instability
515 dynamics, and transient flow responses, Journal of Geophysical Research: Atmospheres,
516 125, 2020.

517 Drob, D. P., Emmert, J. T., Meriwether, J. W., Makela, J. J., Doornbos, E., Conde, M., et al. An
518 update to the Horizontal Wind Model(HWM): The quiet time thermosphere, Earth and
519 Space Science, 2, 301–319, 2015.

520 [Duncombe, J.: The surprising reach of Tonga’s giant atmospheric waves, Eos, 103,](https://doi.org/10.1029/2022EO220050)
521 [https://doi.org/10.1029/2022EO220050, 2022.](https://doi.org/10.1029/2022EO220050)

522 Franke, P. M. and Robinson, W. A.: Nonlinear behavior in the propagation of atmospheric
523 gravity waves, J. Atmos. Sci., 56, 3010-3027, 1999.

524 Fritts, D. C. and Alexander, M. J.: Gravity wave dynamics and effects in the middle
525 atmosphere, Rev. Geophys.,41(1), 1003, 2003.

526 Fritts, D. C., Vadas, S. L., Wan, K., and Werne J. A.: Mean and variable forcing of the middle
527 atmosphere by gravity waves, J. Atmos. Sol. Terr. Phys., 68, 247–265, 2006.

528 Fritts, D. C., B. Laughman, T. S. Lund, and Snively, J. B.: Self-acceleration and instability of
529 gravity wave packets:1. Effects of temporal localization, J. Geophys. Res. Atmos., 120,
530 8783–8803, 2015.

531 Fritts, D. C., Dong, W., Lund, T. S., Wieland, S., and Laughman, B.: Self - acceleration and
532 instability of gravity wave packets: 3.Three - dimensional packet propagation,
533 secondary gravity waves, momentum transport, and transient mean forcing in tidal winds,
534 Journal of Geophysical Research: Atmospheres, 125, 2020.

535 Garcia, F. J., Taylor, M. J., and Kelly, M. C.: Two - dimensional spectral analysis of
536 mesospheric airglow image data, *Applied Optics*, 36(29), 7374–7385,1997.

537 Gavrilov, N. M. and Kshevetskii, S. P.: Features of the Supersonic Gravity Wave Penetration
538 from the Earth's Surface to the Upper Atmosphere, *Radio physics and Quantum*
539 *Electronics*, 61(4), 243-252, 2018.

540 Heale, C. J., Snively, J. B., Bhatt, A. N., Hoffmann, L., Stephan, C. C., and Kendall, E. A.:
541 Multilayer observations and modeling of thunderstorm-generated gravity waves over the
542 Midwestern United States. *Geophysical Research Letters*, 46, 14,164–14,174.
543 <https://doi.org/10.1029/2019GL085934>, 2019.

544 Heale, C. J., Bossert, K., Vadas, S. L., Hoffmann, L., Dornbrack, A., Stober, G., et al.
545 Secondary gravity waves generated by breaking mountain waves over Europe, *Journal*
546 *of Geophysical Research: Atmospheres*,125, e2019JD031662, 2020.

547 Heale, C. J., Inchin, P. A., and Snively, J. B.: Primary Versus Secondary Gravity Wave
548 Responses at F-Region Heights Generated by a Convective Source,*Journal of*
549 *Geophysical Research: Space Physics*, <https://doi.org/10.1029/2021JA029947>, 2021.

550 Hersbach, H., Bell, B., Berrisford, P., Hirahara, S., Horányi, A., Muñoz-Sabater, J., Nicolas, J.,
551 Peubey, C., Radu, R., Schepers, D., Simmons, A., Soci, C., Abdalla, S., Abellan, X.,
552 Balsamo, G., Bechtold, P., Biavati, G., Bidlot, J., Bonavita, M., De Chiara, G., Dahlgren,
553 P., Dee, D., Diamantakis, M., Dragani, R., Flemming, J., Forbes, R., Fuentes, M., Geer,
554 A., Haimberger, L., Healy, S., Hogan, R. J., Hólm, E., Janisková M., Keeley, S.,
555 Laloyaux, P., Lopez, P., Lupu, C., Radnoti, G., de Rosnay, P., Rozum, I., Vamborg, F.,

556 Villaume, S., and Thépaut, J. N.: The ERA5 global reanalysis, *Q. J. R. Meteorol. Soc.*,
557 146(730), 1999–2049, doi:10.1002/qj.3803, 2020.

558 Hoffmann, L., Günther, G., Li, D., Stein, O., Wu, X., Griessbach, S., Heng, Y., Konopka, P.,
559 Müller, R., Vogel, B. and Wright, J. S.: From ERA-Interim to ERA5: The considerable
560 impact of ECMWF’s next-generation reanalysis on Lagrangian transport simulations,
561 *Atmos. Chem. Phys.*, 19(5), 3097–3214, doi:10.5194/acp-19-3097-2019, 2019.

562 Holton, J.R.: The influence of gravity wave breaking on the general circulation of the middle
563 atmosphere, *J. Atmos. Sci.*,40, 2497–2507,1983.

564 [Kogure, M., Yue, J., Nakamura, T., Hoffmann, L., Vadas, S. L., Tomikawa, Y., Ejiri, M. K.,](#)
565 [and Janches, D.: First direct observational evidence for secondary gravity waves](#)
566 [generated by mountain waves over the Andes. *Geophysical Research Letters*, 47, 2020.](#)

567 [Kim, S.-Y., Chun, H.-Y., and Wu, D. L.: A study on stratospheric gravity waves generated by](#)
568 [Typhoon Ewiniar: Numerical simulations and satellite observations, *J. Geophys. Res.*,](#)
569 [114, D22104, 2009.](#)

570 Li, Q., Xu, J., Yue, J., Yuan, W., and Liu, X.: Statistical characteristics of gravity wave
571 activities observed by an OH airglow imager at Xinglong, in northern China, *Annales*
572 *Geophysicae*, 29 (8), 1401–1410, 2011.

573 Liu, H.-L. and Vadas, S. L.: Large-scale ionospheric disturbances due to the dissipation of
574 convectively-generated gravity waves over Brazil, *J. Geophys. Res. Sp. Phys.*, 118(5),
575 2419–2427, doi:10.1002/jgra.50244, 2013.

576 Liu, H.-L., McInerney, J. M., Santos, S., Lauritzen, P. H., Taylor, M. A., and Pedatella, N.

577 M.: Gravity waves simulated by high-resolution Whole Atmosphere Community
578 Climate Model, *Geophys. Res. Lett.*, 41, 9106–9112, 2014.

579 Liu, H., Ding, F., Yue, X., Zhao, B., Song, Q., Wan, W., Ning, B., Zhang, K.: Depletion and
580 traveling ionospheric disturbances generated by two launches of China's Long March 4B
581 rocket. *Journal of Geophysical Research: Space Physics*, 123, 10,319–10,330, 2018.

582 Lund, T. S. and Fritts, D. C.: Numerical simulation of gravity wave breaking in the lower
583 thermosphere, *J. Geophys. Res. Atmos.*, 117, D21105, 10.1029/2012jd017536, 2012.

584 Lund, T. S., Fritts, D. C., Wan, K., Laughman, B., and Liu, H.-L.: Numerical Simulation of
585 Mountain Waves over the Southern Andes. Part I: Mountain Wave and Secondary Wave
586 Character, Evolutions, and Breaking, *Journal of the Atmospheric Sciences*, 77(12),
587 4337-4356, 2020.

588 Pfeffer, R. L. and Zarichny, J.: Acoustic-Gravity Wave Propagation from Nuclear
589 Explosions in the Earth's Atmosphere, *J. Atmos. Sci.* 19, 256–263, 1962.

590 Picone, J. M., Hedin, A. E., Drob, D. P., and Aikin, A. C. NRLMSISE - 00 empirical model of
591 the atmosphere: Statistical comparisons and scientific issues, *Journal of Geophysical*
592 *Research*, 107(A12), 1468, 2002.

593 Pierce, A.D., J. W. Posey, and Iliff, E. F.: Variation of nuclear explosion generated
594 acoustic-gravity wave forms with burst height and with energy yield, *J. Geophys. Res.*,
595 76, 5025-5042, 1971.

596 Sentman, D. D., Wescott, E. M., Picard, R. H., Winick, J. R., Stenbaek-Nielsen, H. C.,

597 Dewan, E. M., Moudry, D. R., Sao Sabbas, F. T., Heavner, M. J., and Morrill, J.:
598 Simultaneous observations of mesospheric gravity waves and sprites generated by a
599 midwestern thunderstorm, *J. Atmos. Sol. Terr. Phys.*, 65, 537–550, 2003.

600 Smith, S. M., Vadas, S. L., Baggaley, W. J., Hernandez, G., and Baumgardner, J.: Gravity
601 wave coupling between the mesosphere and thermosphere over New Zealand, *Journal of*
602 *Geophysical Research: SpacePhysics*, 118, 2694–2707, 2013.

603 Smith, S. M., Setvák, M., Beletsky, Y., Baumgardner, J., and Mendillo, M.: Mesospheric
604 gravity wave momentum flux associated with a large thunderstorm complex, *Journal of*
605 *Geophysical Research: Atmospheres*, 125, e2020JD033381, 2020.

606 Snively, J. B.: Nonlinear [gravity wave forcing as a source of acoustic waves in the](#)
607 [mesosphere, thermosphere, and ionosphere, *Geophysical Research Letters*, 44,](#)
608 [12,020–12,027, 2017.](#)

609 Suzuki, S., Shiokawa, K., Otsuka, Y., Ogawa, T., Nakamura, K., and Nakamura, T.: A
610 concentric gravity wave structure in the mesospheric airglow images, *J. Geophys.*
611 *Res.*, 112, D02102, 2007.

612 Suzuki, S., Vadas, S. L., Shiokawa, K., Otsuka, Y., Kawamura, S., and Murayama, Y.:
613 Typhoon-induced concentric airglow structures in the mesopause region, *Geophys. Res.*
614 *Let.*, 40, 5983–5987, 2013.

615 Taylor, M. J. and Hapgood, M. A.: Identification of a thunderstorm as a source of short period
616 gravity waves in the upper atmospheric nightglow emissions, *Planet. Space Sci.*, 36,
617 975–985, 1988.

618 Vadas, S. L., Fritts, D. C., and Alexander, M. J.: Mechanism for the generation of secondary
619 waves in wave breaking regions, *Journal of the Atmospheric Sciences*, 60, 194–214,
620 2003.

621 Vadas, S. L. and Fritts, D. C.: Thermospheric responses to gravity waves: Influences of
622 increasing viscosity and thermal diffusivity, *J. Geophys. Res.*, 110, D15103,
623 doi:10.1029/2004JD005574, 2005

624 Vadas, S. L.: Horizontal and vertical propagation and dissipation of gravity waves in the
625 thermosphere from lower atmospheric and thermospheric sources, *Journal of*
626 *Geophysical Research*, 112, A06305, 2007.

627 Vadas, S. L., Yue, J., She, C. Y., Stamus, P., and Liu, A. Z.: A model study of the effects
628 of winds on concentric rings of gravity waves from a convective plume near Fort
629 Collins on 11 May 2004, *J. Geophys. Res.*, 114, 2009.

630 Vadas, S. L. and Crowley, G.: Sources of the traveling ionospheric disturbances observed by
631 the ionospheric TIDDBIT sounder near Wallops Island on 30 October 2007, *Journal of*
632 *Geophysical Research*, 115, A07324, 2010.

633 Vadas, S., Yue, J., and Nakamura, T.: Mesospheric concentric gravity waves generated by
634 multiple convective storms over the North American Great Plain, *J. Geophys. Res.*, 117,
635 2012.

636 Vadas, S. L. and Liu, H.-L.: Numerical modeling of the large-scale neutral and plasma
637 responses to the body forces created by the dissipation of gravity waves from 6 h of deep
638 convection in Brazil, *J. Geophys. Res. Sp. Phys.*, 118(5), 2593–2617,

639 doi:10.1002/jgra.50249, 2013.

640 Vadas, S. L., Zhao, J., Chu, X., and Becker, E. The excitation of secondary gravity waves
641 from local body forces: Theory and observation, Journal of Geophysical Research:
642 Atmospheres, 123, 9296–9325, 2018.

643 Vadas, S. L. and Becker, E.: Numerical modeling of the generation of tertiary gravity waves in
644 themosphere and thermosphere during strong mountain wave events over the Southern
645 Andes. Journal of Geophysical Research: Space Physics, 124,7687–7718.
646 <https://doi.org/10.1029/2019JA026694>, 2019.

647 Vadas, S. L. and Azeem, I.: Concentric Secondary Gravity Waves in the Thermosphere and
648 Ionosphere over the Continental United States on 25 - 26 March 2015 from Deep
649 Convection, Journal of Geophysical Research: Space Physics,126, e2020JA028275,
650 2021.

651 Walterscheid, R. L. and Hecht, J. H.: A reexamination of evanescent acoustic-gravity waves:
652 Special properties and aeronomical significance, J. Geophys. Res., 108(D11), 4340,
653 doi:10.1029/2002JD002421, 2003.

654 Xu, J., Li, Q., Yue, J., Hoffmann, L., Straka, W. C., Wang, C., Liu, M.,Yuan,W., Han, S.,
655 Miller, S.D., Sun, L., Liu, X., Liu, W., Yang, J., and Ning, B.: Concentric gravity waves
656 over northern China observed by an airglow imager network and satellites, J. Geophys.
657 Res. Atmos.,120, 11,058–11,078, 2015.

658 Xu, J., Li, Q., Sun, L., Liu, X., Yuan, W., Wang, W., Yue, J., Zhang, S., Liu, W., Jiang, G., Wu,
659 K., Gao, H., and Lai, C.: The Ground - Based Airglow Imager Network in China:
660 Recent Observational Results, Geophysical Monograph Series, 261, 365-394, 2021.

661 Xu, S., Yue, J., Xue, X., Vadas, S. L., Miller, S. D., Azeem, I., et al. Dynamical coupling
662 between Hurricane Matthew and the middle to upper atmosphere via gravity waves,
663 Journal of Geophysical Research: Space Physics, 124,3589–3608, 2019.

664 Yue, J., Vadas, S. L., She, C. Y., Nakamura, T., Reising, S. C., Liu, H. L., Stamus, P., Krueger,
665 D. A., Lyons, W., and Li, T.: Concentric gravity waves in the mesosphere generated by
666 deep convective plumes in the lower atmosphere near Fort Collins, Colorado, J. Geophys.
667 Res. Atmos., 114(6), 1–12, doi:10.1029/2008JD011244, 2009.

668 Yue, J., Miller, S. D., Hoffmann, L., and Straka, W. C.: Stratospheric and mesospheric
669 concentric gravity waves over tropical cyclone Mahasen: Joint AIRS and VIIRS satellite
670 observations, Journal of Atmospheric and Solar - Terrestrial Physics,119, 83–90, 2014.

671 Zhou, X., Holton, J. R., and Mullendore, G. L.: Forcing of secondary waves by breaking of
672 gravity waves in the mesosphere, J. Geophys. Res. Atmos.,107, 2002.